Analytical solutions for semiconductor luminescence including Coulomb correlations with applications to dilute bismides

ORIAKU, C. I. and PEREIRA, Mauro <http://orcid.org/0000-0002-2276-2095>

Available from Sheffield Hallam University Research Archive (SHURA) at:

https://shura.shu.ac.uk/14602/

Analytical solutions for semiconductor luminescence including Coulomb correlations with applications to dilute bismides

C.I. ORIAKU[1,2] AND M.F. PEREIRA[1*]

[1]*Materials and Engineering Research Institute, Sheffield Hallam University, S1 1WB, Sheffield, United Kingdom*
[2]*Department of Physics, Michael Okpara University of Agriculture, Umudike, P.M.B. 7267, Umuahia, Nigeria*
*Corresponding author: m.pereira@shu.ac.uk

In this paper we introduce analytical solutions of interband polarization, which is the selfenergy of the Dyson equation for the Photon Green's functions and apply them to study photoluminescence of Coulomb correlated semiconductor materials. The accuracy of the easily programmable solutions is proven by consistently explaining the low temperature s-shape of the luminescence peak of dilute bismide semiconductors. The different roles of homogeneous versus inhomogeneous broadening at low and high temperatures are described, as well as the relevance of many body effects, which are in very good agreement with experiments.

OCIS codes: (160.6000   ) semiconductor materials; (300.6470)   Spectroscopy, semiconductors; (300.6270)

http://dx.doi.org//JOSA

1. INTRODUCTION

Photoluminescence is one of the main techniques to understand and develop new materials such as dilute bismides, where the incorporation of a small amount of Bi leads to a large bandgap reduction, making $GaAs_{1-x}Bi_x$ an excellent candidate to extend GaAs-based technology to create tunable mid-infrared laser diodes and detectors [1]. As a matter of fact, recent research suggests that trains of pulses from semiconductor disk lasers, that can be based on both dilute nitrides and bismides, when combined with photoconductors might lead even to THz generation [2,3]. In contrast to dilute nitride systems, where a small amount of nitrogen modifies the conduction bands [4], the corresponding band anticrossing effects in dilute bismides modify the valence bands [5-9]. An interesting feature of these materials is the anomalous energy emission peaks at low temperatures, following an unusual s-shape behaviour that is associated with disorder and localization effects, which have been seen in both dilute bismides [8] and nitrides [4]. A simple and efficient method to describe this and other light emission effects in those materials is missing and we propose analytical solutions for the Photon Green's functions approach [10-12], delivering a microscopic, fully quantum mechanical solution. Note that, in spite of its success to accurately explain experiments such as both single beam and nonlinear pump-probe photoluminescence [13], as well as being a powerful tool to design optical devices and solar cells [14] and multi-photon absorption [15], the method usually requires intensive numerical methods. Therefore, in this paper, we aim at two goals: first we deliver analytical solutions of the Dyson equations for the Photon

Green's functions to study photoluminescence of Coulomb correlated semiconductor materials. In contrast to previous approaches, our formalism does not require large numerical inversion schemes or Monte Carlo simulations, which have been applied to explain the (Stokes) shift between emission and absorption [16]. Second, the accuracy of the easily programmable solutions is proven by means of a consistent description of the luminescence spectra and the low temperature s-shape of the luminescence peak of dilute bismide semiconductors as function of scattering mechanisms. The different roles of homogeneous versus inhomogeneous broadening at low and high temperatures are explained as well as the relevance of many body effects in very good agreement with experiments. We explain the disappearance of the s-shape with decreasing homogeneous broadening, which can be attributed to different scattering channels such as electron-electron, electron-phonon, electron-impurity and electron-alloy disorder scattering. This is consistent with recent experimental findings in which rapid thermal annealing improves the sample quality and reduces scattering mechanisms that contribute to the broadening, thus reducing the measured s-shape-like features in InAsN(Sb) samples [17]. Furthermore, it has been recently found experimentally that the addition of antimony reduces the broadening of Photo luminescence emission and Photo reflectance resonances [18]. This has been attributed to an improvement of the alloy quality after antimony incorporation due to its reactive surfactant properties [19, 20]. The scattering processes cited above can all be described by selfenergies [21, 22]. The real and imaginary parts of the retarded selfenergies lead respectively to energy shifts (bandgap re normalisation) and to the dephasing that characterises homogeneous broadening. Depending on the approximation used for the scattering

mechanisms, the resulting expressions may become sufficiently complex. Furthermore, the different samples had quite different levels of residual scattering, due to imperfections and impurities. Thus even if we had used the selfenergies in Ref. [21, 22], parameters would have to be adjusted. Thus, since one of our main goals is to deliver expressions simple enough to be easily programmed by a broad audience, we describe dephasing/scattering globally by a simple density and anisotropy parameter Γ, given in Appendix D. Note however that, even though this reduces the fully microscopic approach, we are fully able to explain the origin of e.g. the s-shape in luminescence spectra. In our approach stronger disorder translates mostly into larger alloy disorder scattering that increases the homogeneous broadening described by the parameter Γ in the equations that follow. Our analytical solutions can thus simply and elegantly explain the evolution of the luminescence spectra as function of excitation, temperature and increasing level of disorder. This paper is organized as follows. We start with the equations in Ref. [11] and outline the derivation of analytical approximations, which are possible due to the screened Coulomb potential chosen. Next, we reproduce experimental luminescence from a number of independent teams with very good accuracy. A short summary follows. We focus on bulk dilute bismides, but superlattices can also in many cases be described with this formalism by treating them as anisotropic bulk media [23].

2. MATHEMATICAL FORMALISM

The quantum mechanical Poynting vector describing light emission can be expressed in terms of the Photon Green's Function, leading to the optical power density spectrum, which can be directly compared with photoluminescence experiments [10,11],

$$I(\omega) = \hbar\omega^2/4\pi^2 ci P^<(\omega). \tag{1}$$

The transverse polarisation function P is the selfenergy in the Dyson equation for the Photon Green's Function and the lesser Keldysh component $P^<$ is proportional to the carriers recombination rate, while P^r is related to absorption/gain and refractive index change. To find analytical solutions, we start by following the step by step procedure in Ref. [11], where only numerical solutions are given and approximate the full frequency dependent population inversion factor by $\vartheta = \tanh\big(\beta(\hbar\omega - \beta\mu)\big)$. Under quasi-equilibrium in each band, the occupation functions are characterized by chemical potentials, μ_e and $\mu_h, \mu = \mu_e + \mu_h$. Homogeneous broadening is accounted through Γ which is the dephasing due to the various possible scattering channels. The material resonance energy is $\Delta e(k) = \frac{\hbar^2 k^2}{2m_r} + E_g$, where $1/m_r = 1/m_e + 1/m_h$. The bandgap E_g is given by the sum of the fundamental band gap E_g^0, and a many body renormalisation term ΔE_g. The integro-differential equation for $P^<$ reduces to

$$P^<(\omega) = \frac{-i 8\pi|\Pi|^2}{\Omega} Im\big\{\sum_{\vec{k}} \Lambda(k, \omega)\big\}, \tag{2}$$

$$(\hbar\omega - \Delta e(k) + i\Gamma)\Lambda(k, \omega) + \sum_{\vec{k'}} \mathcal{W}_{\vec{k} - \vec{k'}} \Lambda(k', \omega) = \mathfrak{B}(\omega), \tag{3}$$

where Π is the matrix element of the velocity operator. Numerical complications due to the singularity introduced by the Kubo-Martin-Schwinger (KMS) relation [11], are eliminated exactly because the resulting factor $\mathfrak{B}(\omega) = 1/\big(1 + exp(\beta(\hbar\omega - \mu))\big)$ is positive and finite, where $\beta = \frac{1}{K_B T}$. The Yukawa potential is the approximation typically used for the screened potential in 3D. However, the corresponding Schrödinger equation does not have known analytical solutions. In contrast, the Hulthén potential, $\mathcal{W}(r) = -2e^2 \kappa \epsilon_0'^{-1}/$

$((\exp(2\kappa r) - 1))$ has known analytical solutions which have successfully reproduced bulk nonlinear absorption spectra [32]. We thus used it here for luminescence calculations. Its three-dimensional Fourier transform also has an analytical expression,

$$\mathcal{W}_q = -\frac{2\pi e^2}{\Omega \epsilon_0' \kappa q} Im\left\{\psi'(1 + \frac{iq}{2\kappa})\right\}, \tag{4}$$

where Ω is the sample volume, ψ' is the Trigamma function [24], κ is the screening wavenumber and $\epsilon_0' = \epsilon_0/\vartheta$. Analytical approximations for μ and κ are given in Appendix A. The bandgap renormalisation including Coulomb hole and screened exchange corrections reads

$$\Delta E_g = -\frac{e^2 \kappa}{\epsilon_0'} - \sum_q \mathcal{W}_q \big(f_e(q) + f_h(q)\big), \tag{5}$$

where the Fermi functions f_e, f_h are evaluated at the peak of the spectral function for each particle. More details are given in Appendix C. This goes beyond previous analytical approaches for absorption in bulk and superlattices that had a phenomenological term for the bandgap shift [23, 25, 26] and also, in contrast to those, here we can take into account a reduction in the Coulomb interaction due to phase space filling through the factor ϑ. Note however that in the range of carrier densities used in the numerical results presented in this paper, $\vartheta \approx 1$ i.e. $\epsilon_0' \approx \epsilon_0$. Next we Fourier-transform Eq. [3] to real space and expand $\Lambda(r, \omega)$ in the basis of eigenstates of the Hamiltonian,

$$-\left[\frac{\hbar^2 \nabla^2}{2m_r} + \mathcal{W}(r)\right] \Psi_\nu(r) = E_\nu \Psi_\nu(r), \tag{6}$$

leading to a closed expression for the output power density,

$$I(\omega) = \frac{4\hbar^2 e^2 |\Pi|^2/c^3}{1 + \exp(\beta(\hbar\omega - \mu))} \sum_\nu |\Psi_\nu(r = 0)|^2 \delta_\Gamma(\hbar\omega - E_g - E_\nu), \tag{7}$$

where $\delta_\Gamma = \frac{1}{\pi} \frac{\Gamma}{(\hbar\omega - E_g - E_\nu)^2 + \Gamma^2}$, but for practical applications, leading to feasible luminescence spectra without the need of a frequency and momentum dependent dephasing, we replace it by any other analytical representation of the Dirac delta function to which it reduces for $\Gamma \to 0$. We choose $\delta_\Gamma(x) = 1/\pi\Gamma \cosh(x/\Gamma)$ (see Appendix B).

Real space representations of the Hulthén potential eigenstates are known [23-27] and among the various possibilities, we choose easily programmable forms of the solutions at r=0.

$$I(\omega) = \frac{I_0}{1 + exp(\beta(\hbar\omega - \mu))}\left\{\sum_{n=1}^{\sqrt{g}} \frac{4\pi}{n}\left(\frac{1}{n^2} - \frac{n^2}{g^2}\right)\delta_\Gamma(\xi - e_n) + 2\pi \int_0^\infty \frac{\sinh(\pi g \sqrt{x})}{\cosh(\pi g \sqrt{x}) - \cos(\sqrt{4g - g^2 x})}\delta_\Gamma(\xi - x)dx\right\}, \tag{8}$$

where $I_0 = \frac{\hbar\omega^2 e^2 |\Pi|^2}{\pi e_0 c^3 a_0^3}$, $e_{n = -(n^{-1} - n g^{-1})^2}$, $\xi = (\hbar\omega - E_g)/e_0$, $g = (\kappa a_0)^{-1}$ and a_0, e_0 denote, respectively the exciton Bohr radius and binding energy. When a small fraction of As atoms is replaced by Bi, the resulting fundamental bandgap E_g^0 can be obtained from $\vec{k} \cdot \vec{p}$ bandstructure combined with the valence band anticrossing model for GaAs$_{1-x}$Bi$_x$ alloys. The interaction of the Bi impurity state with the valence band of GaAs can be described by a 4×4 matrix obtained by diagonalising the full 12×12 $\vec{k} \cdot \vec{p}$ free-carrier Hamiltonian [9, 28-30]. Details of the solution are given in Appendix E.

The effect of bismuth ions on the conduction band of GaAs$_{1-x}$Bi$_x$ alloy is taken into account through the virtual crystal approximation. Fluctuations in the alloy composition are described here by a Gaussian distribution in the dilute Bi mole fraction x. If x_0 is the nominal Bi mole fraction, and $I(x, \omega)$ is the expression in Eq. 8, the inhomogeneously broadened spectrum reads

$$I_{inh}(\omega) = \frac{1}{\sqrt{2\pi\sigma}} \int_{x_0-3\sigma}^{x_0+3\sigma} I(x, \omega)\, e^{-\left(\frac{x-x_0}{\sigma}\right)^2} dx. \qquad (9)$$

3. NUMERICAL RESULTS AND DISCUSSION

Figure 1.a shows a comparison of our calculations with experiments for different compositions of dilute bismide and Fig. 1.b depicts the evolution of the spectra for different temperatures to demonstrate that by using standard material parameters taken from the literature, together with our many body corrections, we deliver the correct spectra and use the same parameters in all other curves. Our theory is predictive. Furthermore, note that even though inhomogeneous broadening is necessary to obtain the correct spectral shape in Fig.1. and Fig.1.b, it is not used here as a fit parameter for fine tuning of the theory vs experiments comparison, since in all curves shown the same fixed value $\sigma = 0.003$ is used. The choice of homogeneous broadening is explained in Appendix D.
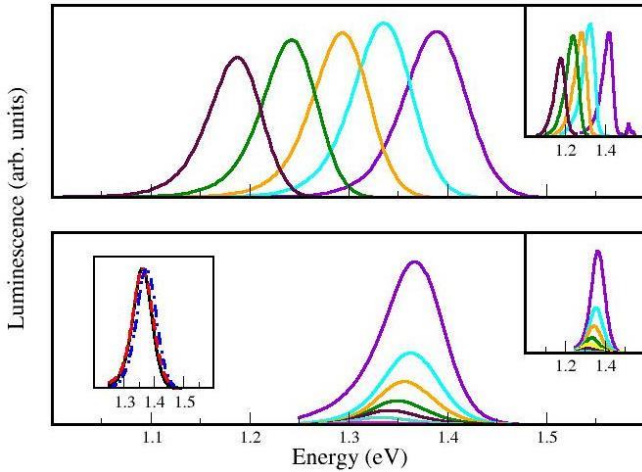

Fig.1. Top panel: Calculated Luminescence spectra of GaAs$_{1-x}$Bi$_x$ on GaAs for different Bi mole fractions, from left to right x=1.16, 1.8, 2.34, 3.04 and 3.83 % fractions at 10 K. The inset depicts experimentally measured data from Ref. [8]. The number of carriers used in the calculation is 10^{15} cm^{-3}. Bottom panel: Calculated Luminescence spectra of GaAs$_{1-x}$Bi$_x$ on GaAs for with a Bi mole fraction x=1.4 %. From top to bottom the temperature is T=150, 175, 200, 225, 250, 275 and 300 K. The right inset depicts experimentally measured data from Ref. [7]. The curves in the left inset compare the following cases: many body calculations (black-solid), experiments (red-dashed) and free carrier calculations (blue-dot-dashed).

Figure 2 depicts the evolution of the luminescence peak energy as a function of temperature, leading to the so called "s-shape" at low temperature. It is clear that many body effects give much better agreement with experiment.
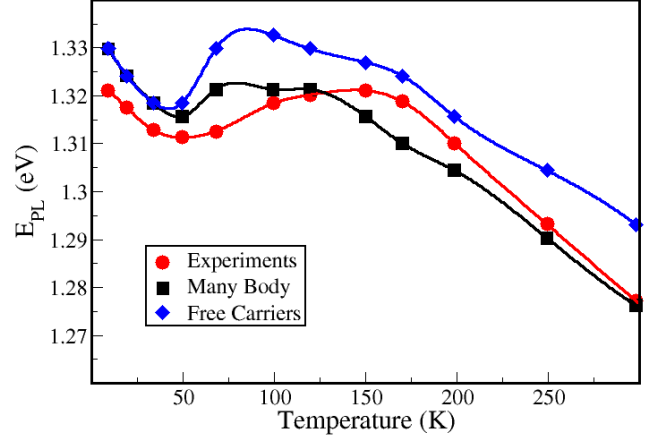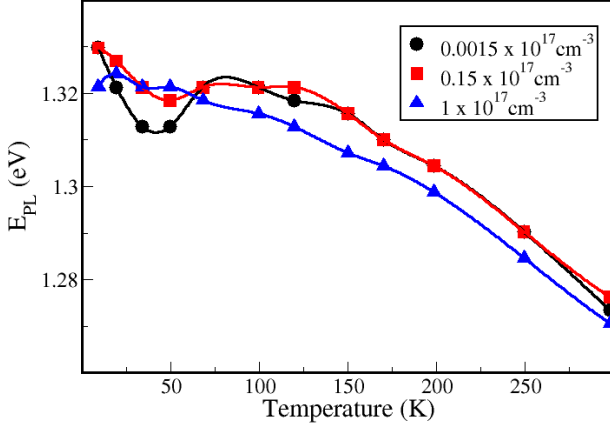

Fig.2. Comparison of luminescence peak energy of GaAs$_{1-x}$Bi$_x$ on GaAs as a function of temperature with experimental data extracted from Ref. [8] (red circles). Comparing our full expressions (black squares) shows the relevance of many body effects against free carrier calculations (blue diamonds). The number of carriers used in the calculation is 10^{15} cm^{-3} and the temperature is 10K.

We attribute the remaining deviations between theory and experiments to the fact that dephasing is actually carrier density, frequency and momentum dependent, while we have used a simple density and anisotropy dependent formula for Γ for all curves. As explained in Appendix A-C a full frequency and momentum dependence would not allow for analytical solutions. Note that a density matrix approach would provide only momentum dependent occupation functions and the steps that allowed the introduction of the frequency dependent θ and $\mathcal{B}$ would not be possible. This justifies using a Green's functions approach. The explicit expression for Γ is given in Appendix D. Figure 3 shows that the "s-shape" feature vanishes with decreasing homogeneous broadening (→ smaller Γ). Thus if scattering channels such as electron-impurity and electron-defect scattering are reduced, e.g. by rapid thermal annealing the feature should accordingly be smaller. This is qualitatively consistent with recent experimental findings in InAsN(Sb) systems, where s-like features disappear with annealing, improving the sample quality [17].
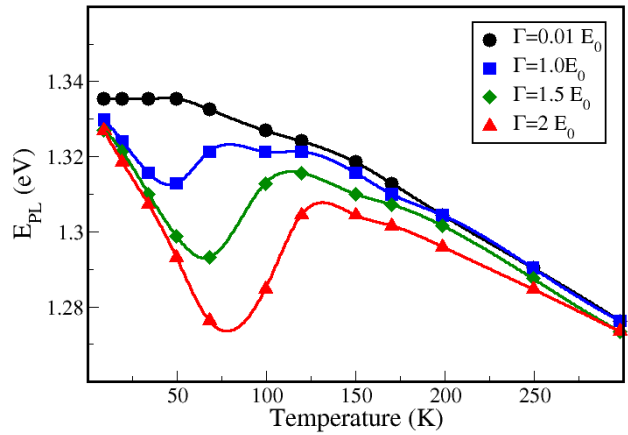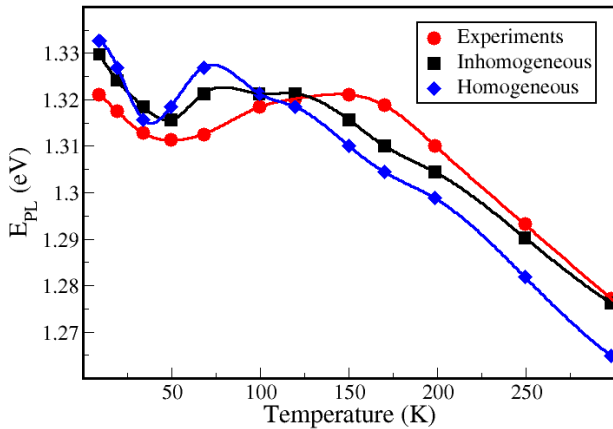

Fig.3. Comparison of luminescence peak energy for the GaAs$_{1-x}$Bi$_x$ on GaAs sample of Fig.2 for increasing homogeneous broadening. The number of carriers used in the calculation is 10^{15} cm^{-3} and the temperature is 10K. From top to bottom, the homogeneous broadening increases by $\Gamma = 0.01, 1, 1.5, 2\, e_0$.

Note also that the s-shape dip towards lower energies for the peak luminescence is predicted only for sufficiently low excitation densities. It vanishes at sufficiently high carrier densities as seen in Fig.4, consistently with experiments [16].

Fig.4. Comparison of luminescence peak energy for the GaAs$_{1-x}$Bi$_x$ on GaAs sample of Figs. 2 and 3 for increasing carrier density. The circles squares and triangles are respectively for increasing carrier density n = 0.0015, 0.15 and 1×10^{17} cm^{-3}.

In other words, by increasing the excitation power, the s-shape disappears. Mathematically the s-shape stems from an interplay between the density dependence and the homogeneous broadening, controlled by the occupation factor. If the chemical potential is removed from our calculations, a Varshni-like plot is obtained i.e. no s-shape. The analysis is completed by clarifying the role of inhomogeneous broadening in Fig.5. Note that, even though inhomogeneous broadening is not the origin of the s-shape, inclusion of some inhomogeneous broadening gives an overall better agreement between theory and experimental spectra and with the peak emission positions. This is consistent with the fact that from fundamental thermodynamics, even high quality alloy samples are expected to have concentration fluctuations [31]. As previously discussed all plots in this paper have the same level of inhomogeneous broadening (σ=0.003),

except of course the (blue-diamonds) curve in Fig.5.
Fig.5. Comparison of luminescence peak energy for the GaAs$_{1-x}$Bi$_x$ on GaAs with experiments from Ref. [8] (red circles). The number of carriers used in the calculations is 10^{15} cm^{-3} and the temperature is 10K. The curves marked by black squares and blue diamonds are calculated respectively with inhomogeneous and homogeneous broadening only.

In summary, in this paper we delivered analytical solutions for the interband polarization function, which is the selfenergy in the Photon Green's function equation and used them for a successful comparison with different types of luminescence experiments from independent research teams. We have shown that the development of an s-shape feature for the peak luminescence can be controlled by the homogeneous broadening and is reduced with increasing excitation power in very good agreement with experiments as well as the interplay between a relatively small amount of alloy fluctuation described by inhomogeneous broadening and many body effects. This illustrates the power of our analytical solutions, which are sufficiently simple to allow a large number of researchers to reproduce and apply them to systematic simulations of experiments for a plethora of new optical materials and devices based on them.

APPENDIX A: Analytical expressions for the chemical potential and inverse screening length

Let's assume that the electron ($\lambda = $ e) and hole ($\lambda = $ h) bands are in quasi-equilibrium with carrier density $n = n_e = n_h$ at temperature T, or equivalently $\beta = 1/(K_B T)$ and thus characterized by chemical potentials μ_e and μ_h. Introducing the dimensionless density μ_λ, a Padé approximation gives [33]

$$\beta\mu_\lambda = ln\nu_\lambda + K_1 \ln(K_2 \nu_\lambda + 1) + K_3 \mu_\lambda. \tag{A1}$$

The screening wavelength is given by $\kappa = \kappa_e + \kappa_h$, where

$$\kappa_\lambda = \sqrt{\frac{4\pi e^2}{\epsilon_0}\frac{\partial n_\lambda}{\partial \mu_\lambda}} = \sqrt{\frac{\beta\pi e^2 n_\lambda/\epsilon_0}{\frac{1}{\nu_\lambda}+\frac{K_1 K_2}{K_2\nu_\lambda+1}+K_3}}, \tag{A2}$$

with $K_1 = 4.897$, $K_2 = 0.045$ and $K_3 = 0.133$. ϵ_0 and e denote, respectively the background dielectric constant and the electron charge and

$$\nu_\lambda = 4n_\lambda/\left[\left(2m_{\parallel,\lambda}/\beta\pi\hbar^2\right)\left(2m_{\perp,\lambda}/\beta\pi\hbar^2\right)^{1/2}\right]. \tag{A3}$$

APPENDIX B: Analytical expressions for the polarisation function

We start from expressions in Refs. [10, 11], simplifed to the two band case

$$P^{r/<}(\omega) = \frac{4\pi e^2|\Pi|^2}{c^2\Omega}\sum_{\vec{k}}\mathcal{P}^{r/<}(k,\omega), \tag{B1}$$

where e, c, Ω and Π denote, respectively the electron charge, the speed of light, the sample volume and the velocity matrix element. The retarded matrix element satisfies the integro-differential equation [11],

$$\mathcal{P}^r(k,\omega) = \mathcal{P}^r_0(k,\omega) - \sum_{\vec{k}}\mathcal{P}^r_0(k,\omega)\mathcal{W}_{\vec{k}-\vec{k}'}\mathcal{P}^r(k',\omega), \tag{B2}$$

where $\mathcal{W}$ is the screened. Furthermore,

$$2Im\{\mathcal{P}^r_0(k,\omega)\} = \int\frac{d\omega'}{2\pi}\hat{G}_e(k,\omega')\,\hat{G}_h(k,\omega-\omega')\{1 - f_e(\omega') - f_h(\omega-\omega')\}. \tag{B3}$$

Under quasi-equilibrium conditions f_λ denotes a Fermi function and spectral function for each particle (electron-e) or (hole-h) reads

$$\hat{G}_\lambda(k,\omega) = \frac{1}{\hbar\omega - e_\lambda(k) + i\Gamma_\lambda}. \tag{B4}$$

Next, we use the relation

$$1 - f_e(\omega') - f_h(\omega - \omega') = \{[1 - f_e(\omega')][1 - f_h(\omega - \omega'] + f_e(\omega')f_h(\omega - \omega')\}\tanh[\beta(\hbar\omega - \mu)/2], \tag{B5}$$

neglecting the term in between braces and evaluating the dephasings at the peak of the corresponding spectral functions, the frequency integration can be performed analytically, leading to

$$\mathcal{P}_0^r(k,\omega) \equiv \frac{\theta}{\hbar\omega - \Delta e(k) + i\Gamma}. \tag{B6}$$

Here, $\mu = \mu_e + \mu_h$. $\Delta e(k) = e_e(k) + e_h(k)$, $\Gamma = \Gamma_e + \Gamma_h$ and $\theta = \tanh[\beta(\hbar\omega - \mu)/2]$. The equation for $\mathcal{P}^r(k,\omega)$ reduces to

$$(\hbar\omega - \Delta e(k) + i\Gamma)\mathcal{P}^r(k,\omega) + \theta\sum_{\vec{k}'}\mathcal{W}_{\vec{k}-\vec{k}'}\mathcal{P}^r(k,\omega) = \theta. \tag{B7}$$

Using the version of the KMS relation derived in Ref. [11],

$$P^<(\omega) = \frac{-2i\,Im\{P^r(\omega)\}}{1 - \exp[\beta(\hbar\omega - \mu)]}, \tag{B8}$$

and introducing the auxiliary variable

$$\Lambda(k,\omega) = \frac{\mathcal{P}^r(k,\omega)}{1 - \exp[\beta(\hbar\omega - \mu)]}, \tag{B9}$$

leads to the relation $\mathcal{P}^<(k,\omega) = -2i\{\Lambda(k,\omega)\}$, and the corresponding integro-differential equation

$$(\hbar\omega - \Delta e(k) + i\Gamma)\Lambda(k,\omega) + \theta\sum_{\vec{k}'}\mathcal{W}_{\vec{k}-\vec{k}'}\Lambda(k,\omega) = \mathcal{B}, \tag{B10}$$

where $\mathcal{B} = -\frac{\tanh[\beta(\hbar\omega - \mu)/2]}{1 - \exp[\beta(\hbar\omega - \mu)]} = \frac{1}{1 + \exp[\beta(\hbar\omega - \mu)]}$.

Note that all numerical difficulties with typical applications of the KMS relation, such as the division by two small numbers are eliminated since $\mathcal{B}$ is always a positive number. Previous work has used a matrix numerical inversion technique to solve the equation for the retarded polarization for the absorption with further use of the KMS relation, successfully describing both single beam and pump and probe luminescence of quasi-two dimensional quantum wells [11, 12]. In contrast we show here an exact analytical solution. We start by simplifying the notation, including the phase space filling factor in the dielectric constant $\epsilon'_0 = \epsilon_0/\vartheta$ as in Eq. 4 of the main text for the Hulthén potential.

Next, we make a Fourier transform in a form that preservs units (Ω is the sample volume),

$$f(r) = \frac{\Omega}{(2\pi)^3}\int f_q e^{-i\vec{q}\cdot\vec{r}}d^3q, \qquad f_q = \frac{1}{(2\pi)^3}\int F(r)e^{i\vec{q}\cdot\vec{r}}d^3r, \tag{B11}$$

$$\left[\omega + i\Gamma - E_g + \frac{\hbar^2\nabla^2}{2m_r} + \mathcal{W}(r)\right]\Lambda(r,\omega) = \Omega\mathcal{B}\delta(r), \tag{B12}$$

where $\delta(r)$ denotes the Dirac delta function. Next, we expand $\Lambda(r,\omega)$ in the basis of eigenstates of the Hamiltonian,

$$-\left[\frac{\hbar^2\nabla^2}{2m_r} + \mathcal{W}(r)\right]\psi_\nu(r) = E_\nu\psi_\nu(r), \qquad \Lambda(r,\omega) = \sum_\nu a_\nu(\omega)\psi_\nu(r), \tag{B13}$$

leading to

$$\Lambda(r,\omega) = \sum_\nu -\frac{\Omega\mathcal{B}\psi_\nu^*(r=0)}{\hbar\omega - E_g - E_\nu + i\Gamma}\psi_\nu(r). \tag{B14}$$

At this point, we Fourier-transform back to k-space and introduce $\Lambda(\omega) = \sum_{\vec{k}}\Lambda(k,\omega)$, obtaining

$$\Lambda(\omega) = \sum_\nu -\frac{\Omega\mathcal{B}|\psi_\nu(r=0)|^2}{\hbar\omega - E_g - E_\nu + i\Gamma}. \tag{B15}$$

The relations

$$P^<(\omega) = -i\frac{8\pi e^2}{\Omega}|\Pi|^2 Im\{\Lambda(\omega)\} \text{ and } I(\omega) = \hbar\omega^2/4\pi^2 ci P^<(\omega), \text{ yield}$$

$$I(\omega) = \frac{4\hbar\omega^2 e^2|\Pi|^2}{c^3(1 - \exp[\beta(\hbar\omega - \mu)])}\sum_\nu|\psi_\nu(r=0)|^2\delta_\Gamma(\hbar\omega - E_g), \tag{B16}$$

where $\delta_\Gamma = \frac{1}{\pi}\frac{\Gamma}{(\hbar\omega - E_g - E_\nu)^2 + \Gamma^2}$ reduces to a Dirac delta function for $\Gamma \to 0$ and the velocity matrix element is expressed in terms of the dipole moment matrix element and the fundamental bandgap as $|\Pi| = (E_g^0/\hbar)|\langle S|x|X\rangle|$.

At this point we replace the Lorentzian by $\delta_\Gamma(x) = 1/\pi\Gamma\cosh(x/\Gamma)$ for the following reasons: note that even though general conclusions can be drawn Refs. [10, 11] these are based on numerical solutions in 2-D k-space for which no know analytical solution exists. A previous study [34], has shown that in order to obtain realistic looking luminescence spectra, the spectral function $\hat{G}$ must retain its Lorentzian-like form, and a frequency and momentum dependent dephasing must be used. Such dephasing would introduce r-dependent terms when we Fourier transform the polarization equation to real space. These extra terms would lead to a problem without analytical solutions. Furthermore, in order to have a simple parameter Γ and the realistic-looking luminescence spectra, see Fig.1, the hyperbolic secant is necessary. Note that the most successful description of e.g. nonlinear absorption in the 3D case has been obtained with analytical approximations [28, 29]. This cannot be done in a numerical solution because important spatial frequencies (high k-values) would be cut out of the matrix inversion and numerical integrations in k-space. The eigenstates and eigenvalues of the Hulthén potential are known [35] and as the expressions above show, we need solutions that do not vanish at r=0, so after the decomposing into radial and angular parts,

$$\psi_\nu(r) = R_{nl}(r)Y_{nl}(\theta,\phi), \tag{B17}$$

we take l=0. The contribution from bound states reads [35]

$$\sum_\nu|\psi_\nu(r=0)|^2 = \frac{1}{\pi a_0^3}\left(\frac{1}{n^3} - \frac{n}{g^2}\right), \quad E_\nu = -e_0\left(\frac{1}{n^2} - \frac{1}{g}\right)^2. \tag{B18}$$

The integer n runs from 0 to the maximum integer in $\sqrt{g}$, $g = (\kappa a_0)^{-1}$ and a_0, e_0 denote, respectively the exciton Bohr radius and binding energy. The inverse screening length κ is given in Appendix A. The contribution from the continuum is

$$\sum_\nu |\psi_\nu(r=0)|^2 = \frac{1}{\pi a_0^3} \int_0^\infty \frac{\sinh(\pi g\sqrt{x})}{\cosh(\pi g\sqrt{x}) - \cos(\pi\sqrt{4g - g^2 x})} dx, \quad (B19)$$

giving rise to Eq. (8) in the main text, where I_0 and ξ are defined.

$$I(\omega) =$$
$$\frac{I_0}{1 + exp(\beta(\hbar\omega - \mu))} \left\{ \sum_{n=1}^{\sqrt{g}} \frac{4\pi}{n} \left(\frac{1}{n^2} - \frac{n^2}{g^2} \right) \delta_\Gamma(\xi - e_n) \ 2\pi \int_0^\infty \frac{\sinh(\pi g\sqrt{x})}{\cosh(\pi g\sqrt{x}) - \cos(\sqrt{4g - g^2 x})} \delta_\Gamma(\xi - x) dx \right\}. \quad (B20)$$

APPENDIX C: Bandgap shift with the Hulthén potential

The poles of the spectral function $\widehat{G}$ occur for each particle λ at $e_\lambda(k) = \frac{\hbar^2 k^2}{2m_\lambda} + E_g^0 \delta_{\lambda,c} + Re\{\Sigma_\lambda^r\}$.

Within the random phase approximation and using a statically screened potential, the following approximation is possible for the real part of the retarded selfenergy.

$$Re\{\Sigma_\lambda^r\} = \Sigma_{exc,\lambda}^r + \Sigma_{CH,\lambda}^r,$$

$$\Sigma_{exc,\lambda}^r = -\sum_q \mathcal{W}_q f_\lambda(q), \quad (C1)$$

$$\Sigma_{CH,\lambda}^r = \frac{1}{2} \lim_{r \to 0}(\mathcal{W}(r) - V(r)) = -\frac{e^2 \kappa}{2\epsilon_0},$$

leading to Eq. 5 in the main text. Thus the bandgap is

$$E_g = E_g^0 + \Delta E_g, \quad (C2)$$

where E_g^0 is the fundamental bandgap found in tables of material properties of semiconductors and

$$\Delta E_g = -\frac{e^2 \kappa}{\epsilon_0'} - \sum_q \mathcal{W}_q (f_e(q) + f_h(q)), \quad (C3)$$

where the fermi functions are evaluated at the peak of the spectral function for each particle. Note that the fundamental bandgap for the electrons and the bandgap shift in each band cancels out with the corresponding correction to the chemical potential.

Thus

$$f_\lambda(q) = \frac{1}{exp\left(\beta\left(\frac{\hbar^2 q^2}{2m_\lambda} - \mu_\lambda\right)\right) + 1}, \quad (C4)$$

with chemical potentials given in Appendix A.

APPENDIX D: Density and anisotropy-dependent dephasing

In all curves and for all temperatures we have used the same phenomenological dephasing that depends on the anisotropy through the binding energy e_0 given by

$$\Gamma = [\Gamma_0 + \Gamma_1 \, ^n/_{n_0}] \cdot e_0, \quad \Gamma_1 = \begin{cases} 2 \times 10^{-23}, & ^n/_{n_0} < 1 \\ 2 \times 10^{-24}, & ^n/_{n_0} \geq 1 \end{cases} \quad (D1)$$

and $n_0 = 10^{15}$ cm^{-3}. In all Fig.1a and its inset and Figs. 2 and 4, $\Gamma_0 = 1$. In Fig.1.b and its insets that corresponding to a different sample with larger residual low density broadening, $\Gamma_0 = 2$. In Fig.3 the total homogeneous broadening Γ is increased arbitrarily to demonstrate its influence in the s-shape.

APPENDIX E: Bandstructure

The interaction of the Bi impurity state with the valence band of GaAs can be described by a 4×4 matrix obtained by diagonalising the full 12×12 $\vec{k} \cdot \vec{p}$ Hamiltonian [9, 28-30].

$$\begin{pmatrix} H & 0 & V_{Bi} & 0 \\ 0 & L & 0 & V_{Bi} \\ V_{Bi} & 0 & E_{Bi} & 0 \\ 0 & V_{Bi} & 0 & E_{Bi-SO} \end{pmatrix}, \quad (E1)$$

where H and L denote the valence band energy for the heavy and the light holes of the GaAs binary semiconductor. The solution of the above matrix equation yields four distinct energy levels heavy/light hole $E_{hh/lh\pm}$ and spin orbit split-off $E_{SO\pm}$ energies [9]. The impurity levels of the heavy or light holes, and the spin orbit split off below the valence band maximum are given, respectively by $E_{Bi} = 0.4$ eV and $E_{Bi-SO} = 1.9$ eV [28]. The matrix element describing the coupling between the Bi- impurity level and the valence bands is $V_{Bi} = C_{Bi}\sqrt{x}$ with $C_{Bi} = 1.6$ eV [9, 25-27].

$$H = -\frac{\hbar^2}{2m_0}\left[(k_x^2 + k_y^2)(\gamma_1 + \gamma_2) + k_z(\gamma_1 - 2\gamma_2)\right] + \Delta E_{VBM}x,$$

$$L = -\frac{\hbar^2}{2m_0}\left[(k_x^2 + k_y^2)(\gamma_1 - \gamma_2) + k_z(\gamma_1 + 2\gamma_2)\right] + \Delta E_{VBM}x. \quad (E2)$$

The distinct energy levels that result from the valence anticrossing are thus

$$E_{hh/lh} = \frac{1}{2}\left(H/L + E_{Bi} \pm \sqrt{(H/L + E_{Bi})^2 + 4V_{Bi}^2}\right), \quad V_{Bi} = C_{Bi}\sqrt{x}. \quad (E3)$$

Note that at high symmetry point $k = 0, H = L$ and that the dilute GaAsBi alloy band gap is given by

$$E_{g,GaAsBi} = E_{g,GaAs} - \Delta E_{CBM}x. \quad (E4)$$

ΔE_{VBM} and ΔE_{CBM} are the difference in valence and conduction band maximum between the GaAs and GaBi binaries. Their values have been obtained earlier as 0.8 and -2.1 eV respectively [9] through model solid theory. The effective masses of the degenerate bands are

$$\frac{1}{m_{hh,lh[GaAs_{1-x}Bi_x]\pm}^*} = \frac{1}{2m_{hh,lh[GaAs]}^*}\left\{\frac{E_{Bi} - H/L}{\sqrt{4V_{Bi}^2 + [E_{Bi} - H/L]^2}} \mp 1\right\}$$

$$m_{hh,lh[GaAs]}^* = (\gamma_1 \mp 2\gamma_2)^{-1} \quad (E5)$$

$$E_{GaAs} = 1.519 + \frac{5.41 \times 10^{-4} \times T^2}{T + 204} \quad (E6)$$

The remaining needful parameters are given in Table I below

Table I. Material parameters

m_e	γ_1	γ_2	ϵ_r	ϵ_∞	C_{Bi}(eV)
0.067	6.98	2.06	13.71	10.89	1.7

References

1. Mircea Guina, Antti Härkönen, Ville-Markus Korpijärvi, Tomi Leinonen, and Soile Suomalainen, "Semiconductor Disk Lasers: Recent Advances in Generation of Yellow-Orange and Mid-IR Radiation", Advances in Optical Technologies, 265010.1-19 (2012).

2. E. J. Saarinen, A. Rantamäki, A. Chamorovskiy, and O. G. Okhotnikov, " "200 GHz 1 W semiconductor disc laser emitting 800 fs pulses", Electron. Lett. 48 (21), 1355–1356 (2012).

3. B. Ferguson and X.C. Zhang, "Materials for terahertz science and technology", Nature materials 1, 26 (2002).

4. A. Krier, M. de la Mare, P.J. Carrington, M. Thompson, Q. Zhuang, A. Patané, and R. Kudrawiec, "Development of dilute nitride materials for mid-infrared diode lasers", Semicond. Sci. Technol. 27, 094009 (2012).

5. C.A. Broderick, M. Usman, S.J. Sweeney and E.P O'Reilly, "Band engineering in dilute nitride and bismide semiconductor lasers ", Semicond. Sci. Technol. 27, 094911 (2012).

6. Y. Gu, K. Wang, H. Zhou, Y. Li, C. Cao, L. Zhang, Y. Zhang, Q. Gong and S. Wang, "Structural and optical characterizations of InPBi thin films grown by molecular beam epitaxy", Nanoscale Research Letters 9, 24, (2014).

7. B. Fluegel, S. Francoeur, A. Mascarenhas, S. Tixier, E. C. Young, and T. Tiedje, "Giant Spin-Orbit Bowing in $GaAs_{1-x} Bi_x$,", Phys. Rev. Lett. 97, 067205 (2006).

8. S. Mazzucato, H. Lehec, H. Carrère, H. Makhloufi, A. Arnoult, C. Fontaine, T. Amand and X. Marie, "Low-temperature photoluminescence study of exciton recombination in bulk GaAsBi", Nanoscale Res Lett 9, 19 (2014).

9. K. Alberi, J. Wu, W. Walukiewicz, K. M. Yu, O. D. Dubon, S. P. Watkins, C. X. Wang, X. Liu, Y.-J. Cho, and J. Furdyna, "Valence-band anticrossing in mismatched III-V semiconductor alloys", Phys. Rev. B 75, 045203 (2007).

10. M. F. Pereira, Jr. and K. Henneberger, "Green's functions theory for semiconductor-quantum-well laser spectra", Phys. Rev. B 53, 16485 (1996).

11. M. F. Pereira, Jr. and K. Henneberger, "Microscopic theory for the influence of Coulomb correlations in the light-emission properties of semiconductor quantum wells", Phys. Rev. B 58, 2064 (1998).

12. D. Yu. Vasylyev, W. Vogel, K. Henneberger, T. Schmielau and D.G. Welsch, Phys. Rev. A78, 033837 (2008).

13. P. Michler, M.Vehse, J. Gutowski, M. Behringer, and D. Hommel, M. F. Pereira Jr. and K. Henneberger, "Influence of Coulomb correlations on gain and stimulated emission in (Zn,Cd)Se/Zn(S,Se)/(Zn,Mg)(S,Se) quantum-well lasers", Phys. Rev. B58, 2055 (1998).

14. U. Aeberhard, " Theory and simulation of quantum photovoltaic devices based on the non-equilibrium Green's function formalism", J. Comput. Electron. 10, 394, (2011).

15. C.-G. Duan, Z.-q. Gu, J. Li, D.-s. Wang and S.-F. Ren, "Application of Green's-function technique to the calculation of multiphoton absorption coefficients of crystalline solids", Phys. Rev. B57, 10 (1998).

16. S. Imhof, A. Tränhart, A. Chernikov, M. Koch, N.S. Köster, K. Kolata, S. Chatterjee, S.W. Koch, X. Lu, S.R. Johnson, D.A. Beaton, T. Tiedje and O. Rubel, "Clustering effects in Ga(AsBi)", Appl. Phys. Lett. 96, 131115 (2010).

17. M. Kesaria, S. Birindelli, A.V. Velichko, Q.D. Zhuang, A. Patané, M. Capizzi and A. Krier, "In(AsN) mid-infrared emission enhanced by rapid thermal annealing", Infrared Physics and Technology 68, 138 (2015).

18. M. Latkowska, M. Baranowski, W.M. Linhart, F. Janiaka, J. Misiewicz, N. Segercrantz, F. Tuomisto, Q. Zhuang, A. Krier and R. Kudrawiec, "The influence of nitrogen and antimony on the optical quality of InNAs(Sb) alloys", J. Phys. D: Appl. Phys. 49, 115105 (2016).

19. Q. Zhuang, A. Godenir, A. Krier, G. Tsai and H.H. Lin, "Molecular beam epitaxial growth of InAsN:Sb for midinfrared optoelectronics", Appl. Phys. Lett. 93, 121903 (2008).

20. H.B. Yuen, S.R. Bank, H. Bae, M.A. Wistey and J.S. Harris Jr., "The role of antimony on properties of widely varying GaInNAsSb compositions", J. Appl. Phys. 99, 093504 (2006).

21. A. Wacker, "Semiconductor Superlattices: A model system for nonlinear transport", Phys. Rep. 357, 1 (2002).

22. T. Schmielau and M.F. Pereira, "Nonequilibrium many body theory for quantum transport in terahertz quantum cascade lasers", Appl. Phys. Lett. 95, 231111 (2009).

23. M.F. Pereira Jr., "Analytical solutions for the optical absorption of semiconductor superlattices", Phys Rev B52, 1978 (1995).

24. M. Abramowitz and I. Stegun, Handbook of Mathematical Functions, (Dover Publications,1965).

25. L. Banyai and S.W. Koch, "A simple theory for the effects of plasma screening on the optical spectra of highly excited semiconductors", Z. Phys. B 63, 283 (1986).

26. H. Haug and S.W. Koch, Quantum Theory of the Optical and Electronic Properties of Semiconductors, (World Scientific, 2005).

27. A.G. Sitenko, Lectures in Scattering Theory. International Series on Monographs in Natural Philosophy, Vol. 39 (Pergamon Press, 1971).

28. K. Alberi, O.D. Dubon, W. Walukiewicz, K.M., K. Bertulis and A. Krotkus, "Valence Band Anticrossing in $GaBi_xAs_{1-x}$", Appl. Phys. Lett. 91, 051909 (2007).

29. P. Ludewig, Z.L. Bushell, L. Nattermann, N. Knaub, W. Stolz , K. Volz, "Growth of Ga(AsBi) on GaAs by continuous flow MOVPE", J. Cryst. Growth 396, 95 (2014).

30. P. Carrier and S.-H. Wei, "Calculated spin-orbit splitting of all diamondlike and zinc-blende semiconductors: Effects of $p_{1/2}$ local orbitals and chemical trends", Phys. Rev. B 70, 035212 (2004).

31. G.B. Stringfellow, Organometallic Vapur-Phase Epitaxy: Theory and Practice, Second Edition, (Academic, New York 1998).

32. Y.H. Lee, A. Chavez-Pirson, S.W. Koch, H.M. Gibbs, S.H. Park, J. Morhange, A. Jeffery, N. Peyghambarian, L. Banyai, A.C. Gossard, W. Wiegmann, "Room-temperature optical nonlinearities in GaAs", Phys. Rev. Lett. 57, 2446 (1986).

33. J.B. Joyce and R.W. Dixon, "Analytic approximations for the Fermi energy of an ideal Fermi gas", Appl. Phys. Lett. 31, 354 (1977).

34. M.F. Pereira Jr., "Many Particle Theory for Luminescence in Quantum Wells", Brazilian Journal of Physics 32, 940 (2002).

35. S. Flügge, Practical Quantum Mechanics (Springer, New York, 1974).